Real-Time Observation of Frustrated Ultrafast Recovery from Ionization in Nanostructured SiO_2 Using Laser-Driven Accelerators

J. P. Kennedy,[1] M. Coughlan,[1] C. R. J. Fitzpatrick,[1] H. M. Huddleston,[1] J. Smyth,[1] N. Breslin,[1] H. Donnelly,[1] B. Villagomez-Bernabe,[1] O. N. Rosmej,[2,3] F. Currell,[4] L. Stella,[1,5] D. Riley,[1] M. Zepf,[6,7] M. Yeung,[1] C. L. S. Lewis,[1] and B. Dromey[1,*]

[1]*Centre for Light-Matter Interactions, Department of Physics and Astronomy, Queen's University Belfast, Belfast BT7 1NN, United Kingdom*

[2]*GSI Helmholtzzentrum für Schwerionenforschung GmbH, Planckstraße 1, 64291, Darmstadt, Germany*

[3]*Goethe University Frankfurt, Max-von-Laue-Straße 1, 60438, Frankfurt am Main, Germany*

[4]*The Dalton Cumbria Facility and the School of Chemistry, The University of Manchester, Oxford Rd, Manchester M13 9PL, United Kingdom*

[5]*School of Chemistry and Chemical Engineering, Queen's University Belfast, Belfast BT7 1NN, United Kingdom*

[6]*Helmholtz-Institute Jena, Fröbelstieg 3, 07743 Jena, Germany*

[7]*Friedrich-Schiller-Universität Jena, Physikalisch-Astronomische Fakultät, Max-Wien-Platz 1, 07743 Jena, Germany*

(Received 9 January 2024; revised 11 May 2024; accepted 16 August 2024; published 23 September 2024)

Ionizing radiation interactions in matter can trigger a cascade of processes that underpin long-lived damage in the medium. To date, however, a lack of suitable methodologies has precluded our ability to understand the role that material nanostructure plays in this cascade. Here, we use transient photoabsorption to track the lifetime of free electrons (τ_c) in bulk and nanostructured SiO_2 (aerogel) irradiated by picosecond-scale (10^{-12} s) bursts of x rays and protons from a laser-driven accelerator. Optical streaking reveals a sharp increase in τ_c from < 1 ps to > 50 ps over a narrow average density (ρ_{av}) range spanning the expected phonon-fracton crossover in aerogels. Numerical modeling suggests that this discontinuity can be understood by a quenching of rapid, phonon-assisted recovery in irradiated nanostructured SiO_2. This is shown to lead to an extended period of enhanced energy density in the excited electron population. Overall, these results open a direct route to tracking how low-level processes in complex systems can underpin macroscopically observed phenomena and, importantly, the conditions that permit them to emerge.

DOI: 10.1103/PhysRevLett.133.135001

As the size and complexity of a system grows, hierarchical sets of laws can emerge that define behavior over different resolutions [1]. An excellent illustration of this occurs in many-body physics. As the long-range order of atoms, or a lattice, is established it can spontaneously break the symmetry of free space leading to the emergence of phonons [2]. Gaining direct insight into how such a hierarchy can underpin a system's response is particularly relevant for radiation interactions in matter. This is because the evolution of deposited energy can span spatiotemporal scales ranging from Å(10^{-10} m) to ~cm and fs to > ns and encompass everything from physical to chemical and biological processes [1–10].

A common starting point for models tracking this transition from excitation to equilibrium is the mean free path between collisions,

$$\lambda = \frac{1}{n\sigma}, \tag{1}$$

where n is the number density and σ is the interaction cross section. While Eq. (1) implies that λ scales inversely proportional with n, the possibility of a nonuniform density [8,11,12] calls into question the assumption of σ being independent of n. For example, a heterogeneous distribution can have fundamentally different nanoscopic structure to that of a homogenous density, yet have the same average n [8,12]. This leads to an unavoidable question: how does the heterogeneity, or granularity, of a medium on the nanoscale affect the ultrafast processes that underpin recovery postirradiation? As most media are not homogenous on these spatial scales (defects, disorder, grain boundaries, etc.), developing methods to test the impact of heterogeneity on σ is central to our ability to realize a

*Contact author: b.dromey@qub.ac.uk

comprehensive model of nanoscopic energy transport in irradiated matter [7–15]. From engineering carrier lifetimes in nanostructured electronics deployed in radiation harsh environments [3–5,10] to investigating novel modalities for radiotherapy in health care [6,13], our ability to transform existing technologies will rely on predicting and controlling [3] the evolution of dose on the shortest spatial and fastest temporal scales postirradiation.

In general, multiple models based on λ are cascaded to interpret this dynamic phase in bulk, or extended, media. The initial dose distribution is obtained from the linear energy transfer (or stopping power) of the irradiating species [16,17]. Next, the thermal spike model [10,18,19] can be invoked for the subsequent energy density evolution and thermalization with the background material. A key element for describing these dynamics is the role of collective medium response. This can be approximated using the phonon gas model (PGM), which assumes a quasi-infinite periodic lattice to support delocalized plane-wave vibrational modes, or phonons [2,9,20]. At the same time, for disordered media, discrepancies between PGM predictions and observations for thermal conductivities and vibrational spectra are addressed by invoking phonon localization [21–23].

Unfortunately, these observables typically encompass a broad range of processes averaged over macroscopic regions. This makes their use in understanding how localization affects material response and recovery to ionizing radiation a challenge due to the nascent action of ionizing species in matter occurring on ultrafast and nanoscopic spatiotemporal scales. To overcome this challenge we track recovery time (free carrier lifetime), τ_c, in bulk and nanostructured SiO_2 irradiated by ps pulses of x rays and protons. As they transfer their energy, these ionizing species generate electron spectra with distinctly different average energies that, as a result, interrogate the material response over distinctly different nm length scales. This duality provides a unique tool with which to study how localization of vibrational modes impacts τ_c and, ultimately, represents a test of how changing complexity on the nanoscale affects macroscopic response.

When a relativistically intense laser pulse ($> 10^{18}$ W cm^{-2}) is incident at an oblique angle (30°–45°) onto a μm-scale thick metal foil target, electrons from the front surface are driven through the foil by the strong electric field of the driving laser. This provides the basis for two highly synchronous ultrafast bursts of radiation from a single high-power laser pulse—a bright broadband pulse of Bremsstrahlung x-ray radiation and burst of protons via the target normal sheath acceleration (TNSA) mechanism [24]. While Bremsstrahlung from laser matter interactions is a well-established source of > 10 keV x rays with ps scale duration, only recently have experiments verified that TNSA pulse durations as short as ∼3 ps are possible from the same interactions [25]. Monte Carlo modeling performed using Geant4 [26] shows that protons (≤ 10 MeV) generate dense nanotracks of ionization with average electron energy, E_{av}, < 100 eV. Conversely, x rays (> 10 keV, < 100 keV) undergo multiple high momentum transfer scattering events that homogenize the initial dose distribution and result in E_{av} on the order of 25 keV (see Supplemental Material [27]). The experimental setup is shown in Fig. 1(a). It shows how single-shot optical streaking was performed using the laser-driven accelerator at the TARANIS facility in Queen's University Belfast [25,36] (see Appendix A) to track τ_c following the interaction of these ps-scale pulses in bulk and nanostructured SiO_2 with a range of average densities ρ_{av} [see Figs. 1(b) and 1(c)]. Silica aerogels [37–43] were used composed of a nanostructured matrix of solid density SiO_2 nanoparticles with an average size of $a = 3 \pm 1$ nm and tuneable average pore size [see Fig. 1(d)]. These nanostructured media can be described as a percolating fractal network across spatial scales l_F up to an acoustic correlation length ξ_{ac} (where $a < l_F < \xi_{ac}$[Å]) [40–42] that can be estimated as $8.3 \times 10^6 \times \rho_{av[kg\cdot m^{-3}]}^{-1.84}$ [43] (see Appendix B). In SiO_2, longitudinal optical (LO) phonon emission [44] and polaronic stopping (POL) [45,46] represent the primary mechanisms of energy loss for electrons with average energies (E_{av}) within the subexcitation range in SiO_2. As such, aerogels provide control over heterogeneity on spatial scales relevant for scattering of subexcitation energy electrons from LO phonons (λ_{LO}) in SiO_2 [44].

Optical streaks obtained for x rays followed by slower protons interacting in bulk and a range of nanostructured SiO_2 samples are shown in Figs. 1(b) and 1(c). These materials and densities straddle the transition expected for fractal behavior in nanostructured SiO_2 [43]. As can be seen there is a sharp increase in τ_c for both the x rays and protons interacting in the 0.26 g cm^{-3} aerogel sample. Based on the simplistic $\tau_c \propto \rho_{av}^{-1}$ scaling, one would expect a moderate < 3 times increase in τ_c. Instead, we observe factors of 50–70 times longer in τ_c for both x rays and protons interacting in aerogel.

Figure 2 shows dependence of the recovery time on average density ($\tau_c \propto \rho_{av}^{-1}$), which reveals a sharp discontinuity in the scaling for both protons and x rays. As the material structure changes from root mean square (rms) pore size < 5 nm to rms pore size > 10 nm [Fig. 1(d)], the ultrafast response in SiO_2 due to self-trapped exciton formation (STE) [47] is observed to quench, with $\tau_c <$ ps growing to $\tau_c > 50$ ps (see Appendix C). Importantly, this switching is observed for recovery due to irradiation from both x rays (generating secondary electrons with E_{av} that stop on length scales $\gg \xi_{ac}$) and protons (generating secondary electrons with E_{av} that stop on length scales of a to l_f). As mentioned, E_{av} for electrons due to 10 MeV proton stopping in SiO_2 is on the order tens of eV. In Fig. 4 (based on [44]), λ for these electrons in bulk SiO_2 is < 3 nm. The implication is that the dose due to 10 MeV

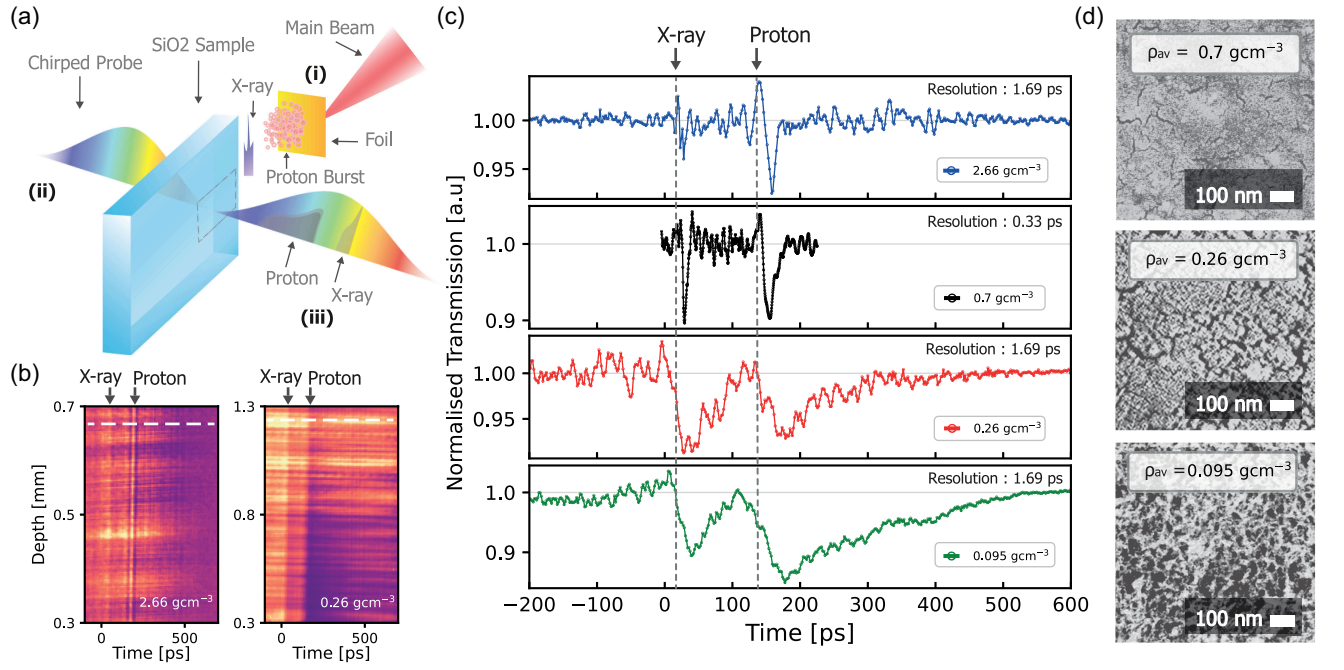

FIG. 1. Spatiotemporally resolved ionisation dynamics for picosecond scale pulses of x rays and protons stopping in bulk and nanostructured SiO_2. Sketch (a) shows the experimental setup: (i) the main laser is incident onto a foil target generating a bright broadband pulse of x-ray radiation and burst of protons via the TNSA mechanism [24]; (ii) a linearly chirped probe synchronized with the main laser is incident onto a sample; (iii) as the chirped probe passes through the sample, the ionization dynamics due to the radiation generated by the main laser are encoded temporally in the observed spectrum of the probe. In (b) experimentally obtained optical streak data for opacity induced in SiO_2 with average densities (ρ_{av}) 2.66 g cm^{-3} (bulk) and 0.26 g cm^{-3} (aerogel) are shown. Plot (c) shows the background subtracted lineouts for interactions in 2.66 g cm^{-3} (bulk, blue dots), 0.7 g cm^{-3} (xerogel, black dots), 0.26 g cm^{-3} (aerogel, red dots), and 0.095 g cm^{-3} (aerogel, green dots) taken from the raw optical streak data [shown in (b)] at the white dashed lines. Data for each sample is obtained on a single shot with its corresponding resolution shown on each plot. Time is given with respect to the time of the laser interaction with the foil target. The depths where lineouts are taken are chosen such that the absolute proton pulse duration is at a constant to allow direct comparison (see Supplemental Material [27]). Scanning electron microscope images for samples of various densities are shown in (d). The magnification is 33 000 times, and the scale bar of 100 nm is the same for all images.

proton stopping directly interrogates the nanoscopic heterogeneity in aerogel, which is at bulk density. In contrast, E_{av} due to a bremsstrahlung source with a 50 keV temp is tens of keV. For these electrons in bulk SiO_2 λ is > 100 nm and considerably larger in the lower density samples (blue line in Fig. 4). This is significantly larger than ξ_{ac} predicted by the scaling from [43]. This implies that these electrons probe the medium over length scales on which homogeneous behavior is expected. The interpretation of this is clear: despite the very different E_{av}, the nanostructure of the irradiated medium is dominating the material response and recovery dynamics on ultrafast time frames.

It is important to note that this does not preclude STE formation in general. It simply implies that the time taken to meet the trapping criterion put forward by Martin *et al.* [48] is significantly longer than would be expected if the $\tau_c \propto \rho_{\mathrm{av}}^{-1}$ scaling is applied to the result of Audebert *et al.* [47] (gray dashed line, Fig. 2). To help interpret these observations, we implement a energy transfer model [18,19,49] to track the early stage evolution of the thermal electron population caused by a single proton stopping in bulk SiO_2 and aerogel with $\rho_{\mathrm{av}} = 0.26$ g cm^{-3}.

First, we consider the situation where the cross sections for interactions are independent of structure on the nanoscale. This is given by the solid traces in Figs. 3(a) and 3(b), with red for bulk and blue for nanostructured SiO_2. Figure 3(a) shows that following a rapid diffusion phase (< 0.2 ps), there is a clear effect of the nanostructure in slowing the evolution of electron density, n_e, in aerogel compared to that in bulk SiO_2, with $n_e(\mathrm{bulk}) < n_e(\mathrm{aerogel})$ for τ extending to 50 ps. However, for $\tau > 0.2$ ps in both materials, n_e is below $n_e^{\mathrm{Exciton}} \approx 10^{20}$ cm^{-3}. This is the maximum free carrier density observed for STE formation in SiO_2 from experiments [50]. Accordingly, confinement of a near-solid density population of hot electrons in the nanostructure on its own can be ruled out as the source of enhanced τ_c in aerogel as n_e is below n_e^{Exciton} for both samples. Similarly, Fig. 3(b) reveals a corresponding increase in the kinetic energy density (Ω) for the electron population in nanostructured SiO_2. This increase is largely reconciled by the increase in n_e when it is considered over nm length scales. Therefore, for these conditions, similar E_{av} is expected for electrons ionized by protons stopping in both bulk and nanostructured SiO_2.

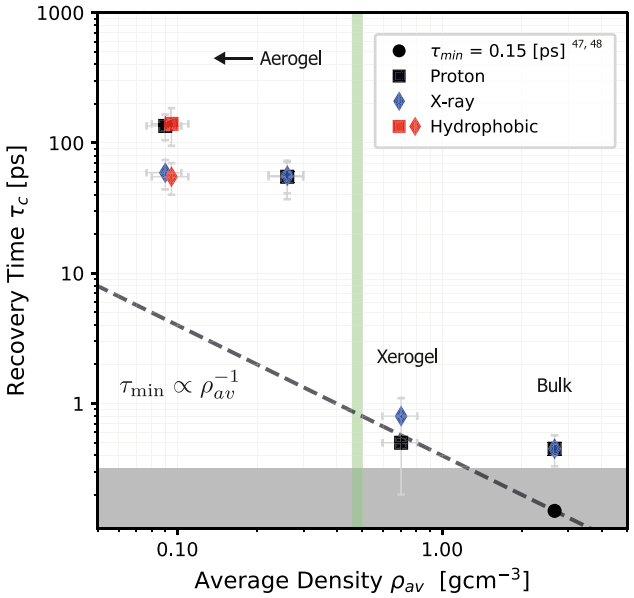

FIG. 2. Dependence of recovery time τ_c on average density (ρ_{av}). As the nanostructure changes from bulk to percolating fractal network a distinct discontinuity in the scaling of τ_c with respect to ρ_{av} is observed. The presence of H_2O as a potential cause for the observed increase in τ_c is removed by using an aerogel sample with hydrophobic surface chemistry (red symbols, density 0.1 g cm^{-3}). The green shaded region outlines the expected boundary between bulk and fractal phenomenology. The black dashed line shows the expected scaling assuming a homogenous reduction in $\rho_{\mathrm{av}}(\tau_{\mathrm{ac}} \propto \rho_{\mathrm{av}}^{-1})$ and is based on the experimentally observed $\tau_{\mathrm{min}} = 0.15$ ps for $\rho_{\mathrm{av}} = 2.66$ g cm^{-3} from Audebert *et al.* [47]. The gray shaded region is the minimum resolution for the optical streaking performed here (0.33 ± 0.05 ps).

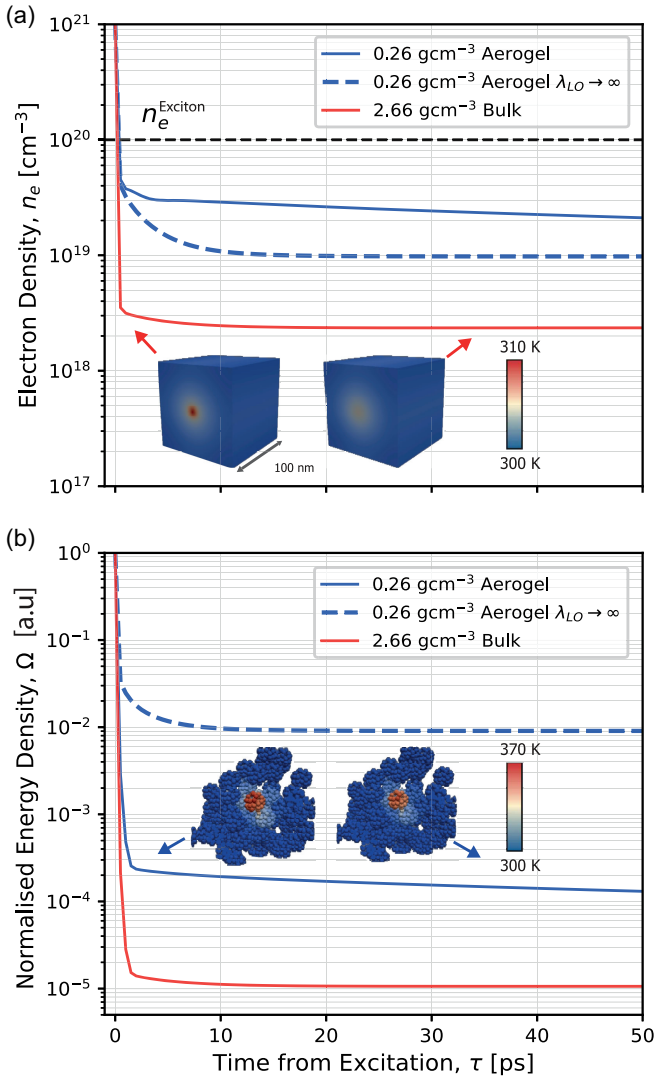

FIG. 3. Hydrodynamic modeling of the hot electron population evolution. In (a) the evolution of the electron density following the interaction of a single proton in bulk and aerogel samples demonstrates a significant increase in electron density over extended time frames. The corresponding normalized energy density is shown in (b) (solid red and blue lines in both figures, respectively), assuming $\lambda \propto \rho_{\mathrm{av}}^{-1}$. Conversely, if $\lambda_{\mathrm{LO}} \to \infty$ is set for aerogel the dashed traces are obtained for the calculations. The figure insets show lattice temperature due to the deposited dose evolves spatially for bulk and nanostructured SiO_2. In both cases, the maximum lattice temperature is significantly lower than both melting (> 1700 K) and Debye temperature (470 K) in SiO_2. For more information on hydrodynamic model see Appendix E.

This suggests that the trapping criterion of Martin *et al.* [48] should not be violated in aerogel for conditions where ultrafast trapping is observed in the bulk sample. As such, our initial assumption of constant σ for both bulk and nanostructured SiO_2 fails to explain for the enhanced τ_c observed in aerogel.

To reconcile this discrepancy, we test how the nanoscopic heterogeneity of the aerogel may lead to the suppression of loss mechanisms for subexcitation energy electrons. Assuming the cross section for LO phonon emission (σ_{LO}^{-}) becomes vanishingly small, i.e., $\lambda_{\mathrm{LO}} \to \infty$ the picture changes considerably. For $\tau > 10$ ps our model suggests $> 10^2$ times increase in Ω over that expected in bulk SiO_2 [blue dash line, Fig. 3(b)]. This implies that the requirement for E_{av} to approach the thermal energy of the lattice for trapping via excitonic states is no longer met on timescales extending to tens of ps. It is only when we impose a restriction on losses through phonon interactions in nanostructured SiO_2 do we see the energy density remain at levels that would violate trapping criterion of Martin *et al.* [48] over extended time frames. To clarify, while the confinement provided by the nanostructure in the aerogel samples provides a moderate increase in n_e, the dramatic boost in Ω required to reconcile our observations only exists under conditions where $\lambda_{\mathrm{LO}} \to \infty$.

The assumption that $\lambda_{\mathrm{LO}} \to \infty$ in aerogel is supported in several ways. First, it does not suggest that vibrations cease to exist in aerogel. The hierarchy of fractons and complex surface modes of the nanoparticles comprising the aerogel substructure can play a key role in the carrier dynamics

postirradiation [37–40,51]. However, when it is considered that electrons with $E_{\mathrm{av}} < 0.9$ eV (electron affinity in SiO_2) [45] are essentially confined in the nanoscopic network [i.e., Fig. 3(a)] this can lead to a nonequilibrium phonon distribution due to a locally enhanced n_e. For these conditions the cross section for absorption of optical phonons (σ^{+}_{LO}) approaches σ^{-}_{LO} approximating to $\lambda_{\mathrm{LO}} \to \infty$ (hot phonon bottleneck) [52]. Second, LO phonons decay into two acoustic phonons on 1 ps timescales [53]. While long-wavelength acoustic modes ($> \xi_{\mathrm{ac}}$) can still propagate in aerogel, albeit at considerably reduced velocity to their bulk counterparts [42], recent work has begun to question the relative stopping powers for optical and short-wavelength acoustic phonons in bulk materials [54]. In aerogel these short wavelength acoustic modes will manifest as fractons with short localization length for l_F ($< \xi_{\mathrm{ac}}$). This implies a significantly reduced spatial overlap with free carriers in aerogel over bulk, subsequently reducing the probability of energy loss [12]. Finally, it is also important to recognize the significance of the quasi-infinite periodic lattice assumed in the PGM. As outlined earlier, the periodicity of the lattice spontaneously breaks the Galilean symmetries of free space leading to the emergence of Higgs and Goldstone modes, or optical and acoustic phonons respectively [2]. Conversely, the nanoscopic self-similarity of fractal networks implies that these systems do not possess the long-range translational symmetry of a crystal lattice, i.e., the assumption of quasi-infinite periodicity is invalid. In this sense, Galilean symmetries are not spontaneously broken in self-similar or fractal materials as they are not translationally invariant [39,40] and the assumption that $\lambda_{\mathrm{LO}} \to \infty$ in aerogels can be grounded in basic symmetry arguments. Although the modeling in Fig. 3 provides a possible insight into the excited electron population dynamics over short distances, the rigorous analysis required to fully interrogate recombination and trapping dynamics for the excited electron population in a numerical framework for this phase is beyond the scope of the work here [55]. See Supplemental Material for more detail on this [27].

In conclusion, this work further supports the idea that the fundamental nature of atomic scale vibrations, and what may be termed coherent phonon modes, must be considered carefully in the context of disordered and nanostructured materials. Our work shows that this is particularly relevant for understanding the evolution of deposited energy due to ionizing radiation in such media. The observation of a sharp discontinuity in the scaling of τ_c for a heterogeneous reduction in ρ_{av} demonstrates that the efficient mechanisms for ultrafast relaxation of subexcitation energy electrons via LO phonon emission is not dominant in aerogels over length scales where both strongly localized ($l_f < \xi_{\mathrm{ac}}$) and delocalized ($L > \xi_{\mathrm{ac}}$) phonon modes are expected. These length scales are probed by primary electrons due to proton and x-ray stopping, respectively. This leads to the conclusion that ultrafast decay of free carriers in SiO_2 emerges as the nanoscale structure of the material is modified to that of a nonfractal medium with long-range (> 5 nm) periodic lattice. Furthermore, this work demonstrates how the multispecies capabilities of laser-driven accelerators can provide a platform for future investigations on the role of anomalous diffusion on fractal networks and in disordered systems in real time. It also provides the potential for highly synchronized harmonic probe beams with attosecond resolution [56] for investigating the fundamental nature of energy loss via electron-phonon interactions (i.e., LO versus acoustic modes) [54] in irradiated materials on the primary excitation timescales.

Acknowledgments—We would like to thank V. P. Efremov for supplying aerogel samples. Work is funded through EPSCR grants (EP/P010059/1, EP/P016960/1, and EP/W017245/1). We are also grateful for use of the computing resources from the Northern Ireland High Performance Computing (NI-HPC) service funded by EPSRC (EP/T022175). L. S. also acknowledges funding from the European Union's Horizon 2020 research and innovation programme under the Marie Skłodowska-Curie Actions staff exchange Grant Agreement No. 823897 (MSCA-RISE "ATLANTIC"). L. S. and J. S. also acknowledgments support from the COST Action CA17126 "TUMIEE."

[1] P. W. Anderson, Science **177**, 393 (1972).
[2] M. Vallone, Phys. Status Solidi (b) **257**, 1900443 (2020).
[3] G. Ackland, Science **327**, 1587 (2010).
[4] M. Coughlan, H. Donnelly, N. Breslin, C. Arthur, G. Nersisyan, M. Yeung, B. Villagomez-Bernabe, M. Afshari, F. Currell, M. Zepf, and B. Dromey, New J. Phys. **22**, 103023 (2020).
[5] M. Mo, S. Murphy, Z. Chen, P. Fossati, R. Li, Y. Wang, X. Wang, and S. Glenzer, Sci. Adv. **5**, eaaw0392 (2019).
[6] R. M. de Kruijff, Int. J. Radiat. Biol. **96**, 419 (2020).
[7] D. G. Cahill, P. V. Braun, G. Chen, D. R. Clarke, S. Fan, K. E. Goodson, P. Keblinski, W. P. King, G. D. Mahan, A. Majumdar, H. J. Maris, S. R. Phillpot, E. Pop, and L. Shi, Appl. Phys. Rev. **1**, 011305 (2014).
[8] M. C. Wingert, J. Zheng, S. Kwon, and R. Chen, Semicond. Sci. Technol. **31**, 113003 (2016).
[9] J. S. Reid, Phys. Educ. **11**, 348 (1976).
[10] M. Toulemonde, W. Assmann, C. Dufour, A. Meftah, and C. Trautmann, Nucl. Instrum. Methods Phys. Res., Sect. B **277**, 28 (2012).
[11] M. U. Siddiqui and A. F. M. Arif, Materials **9**, 694 (2016).
[12] R. Orbach, Science **231**, 814 (1986).
[13] E. Surdutovich and A. V. Solov'yov, Cancer Nanotechnol. **10**, 1 (2019).
[14] G. Tagliabue, J. S. DuChene, M. Abdellah, A. Habib, D. J. Gosztola, Y. Hattori, W.-H. Cheng, K. Zheng, S. E. Canton, R. Sundararaman *et al.*, Nat. Mater. **19**, 1312 (2020).

[15] M. E. Siemens, Q. Li, R. Yang, K. A. Nelson, E. H. Anderson, M. M. Murnane, and H. C. Kapteyn, Nat. Mater. **9**, 26 (2010).

[16] B. Henke, E. Gullikson, and J. Davis, At. Data Nucl. Data Tables **54**, 181 (1993).

[17] J. F. Ziegler, J. Appl. Phys. **85**, 1249 (1999).

[18] S. Klaumünzer, Thermal-spike models for ion track physics: A critical examination, in *Ion Beam Science: Solved and Unsolved Problems*, edited by P. Sigmund (2006), Vol. 52, pp. 293–328, http://publ.royalacademy.dk/books/163/1017?lang=en [Online].

[19] M. Kaganov, Sov. Phys. JETP **4**, 173 (1957), http://www.jetp.ras.ru/cgi-bin/e/index/e/4/2/p173?a=list.

[20] W. Lv and A. Henry, Sci. Rep. **6**, 37675 (2016).

[21] P. W. Anderson, Phys. Rev. **109**, 1492 (1958).

[22] J. E. Graebner and B. Golding, Phys. Rev. B **34**, 5788 (1986).

[23] M. N. Luckyanova, J. Mendoza, H. Lu, B. Song, S. Huang, J. Zhou, M. Li, Y. Dong, H. Zhou, J. Garlow, L. Wu, B. J. Kirby, A. J. Grutter, A. A. Puretzky, Y. Zhu, M. S. Dresselhaus, A. Gossard, and G. Chen, Sci. Adv. **4**, eaat9460 (2018).

[24] A. Macchi, M. Borghesi, and M. Passoni, Rev. Mod. Phys. **85**, 751 (2013).

[25] B. Dromey, M. Coughlan, L. Senje, M. Taylor, S. Kuschel, B. Villagomez-Bernabe, R. Stefanuik, G. Nersisyan, L. Stella, J. Kohanoff *et al.*, Nat. Commun. **7**, 10642 (2016).

[26] S. Agostinelli, J. Allison, K. a. Amako, J. Apostolakis, H. Araujo, P. Arce, M. Asai, D. Axen, S. Banerjee, G. Barrand *et al.*, Nucl. Instrum. Methods Phys. Res., Sect. A **506**, 250 (2003).

[27] See Supplemental Material at http://link.aps.org/supplemental/10.1103/PhysRevLett.133.135001 for additional information, which includes Refs. [28–35].

[28] J. T. Devreese, arXiv:1611.06122.

[29] M. V. Fischetti, D. J. DiMaria, S. D. Brorson, T. N. Theis, Kirtley, and J. R., Phys. Rev. B **31**, 8124 (1985).

[30] C. Li, S. F. Mao, Y. B. Zou, Y. G. Li, P. Zhang, H. M. Li, and Z. J. Ding, J. Phys. D **51**, 165301 (2018).

[31] S. Nagano, M. Tsukiji, K. Ando, E. Hasegawa, and A. Ishitani, J. Appl. Phys. **75**, 3530 (1994).

[32] D. Polli, D. Brida, S. Mukamel, G. Lanzani, and G. Cerullo, Phys. Rev. A **82**, 053809 (2010).

[33] A. Prasselsperger, M. Coughlan, N. Breslin, M. Yeung, C. Arthur, H. Donnelly, S. White, M. Afshari, M. Speicher, R. Yang, B. Villagomez-Bernabe, F. J. Currell, J. Schreiber, and B. Dromey, Phys. Rev. Lett. **127**, 186001 (2021).

[34] B. K. Ridley, *Quantum Processes in Semiconductors*, 5th ed. (Oxford University Press, New York, 2013).

[35] E. Schreiber and H.-J. Fitting, J. Electron Spectrosc. Relat. Phenom. **124**, 25 (2002).

[36] T. Dzelzainis, G. Nersisyan, D. Riley, L. Romagnani, H. Ahmed, A. Bigongiari, M. Borghesi, D. Doria, B. Dromey, M. Makita *et al.*, Laser Part. Beams **28**, 451 (2010).

[37] D. W. Schaefer and K. D. Keefer, Phys. Rev. Lett. **56**, 2199 (1986).

[38] E. Courtens, J. Pelous, J. Phalippou, R. Vacher, and T. Woignier, Phys. Rev. Lett. **58**, 128 (1987).

[39] E. Anglaret, A. Hasmy, E. Courtens, J. Pelous, and R. Vacher, Europhys. Lett. **28**, 591 (1994).

[40] T. Nakayama and K. Yakubo, *Fractal Concepts in Condensed Matter Physics* (Springer, Berlin, Heidelberg, 2003), Vol. 140.

[41] Y. Gefen, A. Aharony, and S. Alexander, Phys. Rev. Lett. **50**, 77 (1983).

[42] S. Caponi, G. Carini, G. D'Angelo, A. Fontana, O. Pilla, F. Rossi, F. Terki, G. Tripodo, and T. Woignier, Phys. Rev. B **70**, 214204 (2004).

[43] E. Courtens, R. Vacher, J. Pelous, and T. Woignier, Europhys. Lett. **6**, 245 (1988).

[44] E. Schreiber and H.-J. Fitting, J. Electron Spectrosc. Relat. Phenom. **124**, 25 (2002).

[45] S. V. Stepanov, Radiat. Phys. Chem. **46**, 29 (1995).

[46] M. Dapor, J. Phys. Conf. Ser. **402**, 012003 (2012).

[47] P. Audebert, P. Daguzan, A. Dos Santos, J. C. Gauthier, J. P. Geindre, S. Guizard, G. Hamoniaux, K. Krastev, P. Martin, G. Petite, and A. Antonetti, Phys. Rev. Lett. **73**, 1990 (1994).

[48] P. Martin, S. Guizard, P. Daguzan, G. Petite, P. D'Oliveira, P. Meynadier, and M. Perdrix, Phys. Rev. B **55**, 5799 (1997).

[49] T. Grasser, T.-W. Tang, H. Kosina, and S. Selberherr, Proc. IEEE **91**, 251 (2003).

[50] C. Mauclair, A. Mermillod-Blondin, K. Mishchik, J. Bonse, A. Rosenfeld, J.-P. Colombier, and R. Stoian, High Power Laser Sci. Eng. **4**, e46 (2016).

[51] E. B. Ramayya, D. Vasileska, S. M. Goodnick, and I. Knezevic, J. Appl. Phys. **104**, 063711 (2008).

[52] Y. Yang, D. P. Ostrowski, R. M. France, K. Zhu, J. Van De Lagemaat, J. M. Luther, and M. C. Beard, Nat. Photonics **10**, 53 (2016).

[53] P. G. Klemens, Phys. Rev. **148**, 845 (1966).

[54] M. V. Fischetti, P. D. Yoder, M. M. Khatami, G. Gaddemane, and M. L. Van de Put, Appl. Phys. Lett. **114**, 222104 (2019).

[55] L. Stella, J. Smyth, B. Dromey, and J. Kohanoff, Eur. Phys. J. D **75**, 1 (2021).

[56] L. Seiffert, Q. Liu, S. Zherebtsov, A. Trabattoni, P. Rupp, M. Castrovilli, M. Galli, F. Süßmann, K. Wintersperger, J. Stierle *et al.*, Nat. Phys. **13**, 766 (2017).

[57] K. McKeever, M. Makita, G. Nersisyan, T. Dzelzainis, S. White, B. Kettle, B. Dromey, M. Zepf, G. Sarri, D. Doria, H. Ahmed, C. L. S. Lewis, D. Riley, and A. P. L. Robinson, Phys. Rev. E **91**, 033107 (2015).

[58] N. Medvedev, B. Ziaja, M. Cammarata, M. Harmand, and S. Toleikis, Contrib. Plasma Phys. **53**, 347 (2013).

[59] J. Ashley and V. Anderson, IEEE Trans. Nucl. Sci. **28**, 4131 (1981).

[60] M. V. Fischetti, Phys. Rev. Lett. **53**, 1755 (1984).

[61] M. Alnæs, J. Blechta, J. Hake, A. Johansson, B. Kehlet, A. Logg, C. Richardson, J. Ring, M. E. Rognes, and G. N. Wells, Arch. Numer. Software **3**, 9 (2015).

[62] V. Morales-Flórez, N. D. L. Rosa-Fox, M. Piñero, and L. Esquivias, J. Sol-Gel Sci. Technol. **35**, 203 (2005).

[63] V. Morales-Flórez, M. Piñero, N. de la Rosa-Fox, L. Esquivias, J. A. Anta, and J. Primera, J. Non-Cryst. Solids **354**, 193 (2008).

[64] C. Geuzaine and J.-F. Remacle, Int. J. Numer. Methods Eng. **79**, 1309 (2009).

End Matter

Appendix A: Ultrafast sources on TARANIS and single-shot optical streaking—Ultrafast laser-driven x-ray and proton sources are generated on TARANIS via interaction of a 1053 nm, 800 fs laser pulse ($2 \pm 1 \times 10^{19}$ W cm^{-2}, contrast $\sim 10^{-7}$, ~ 2 ns before main pulse) at 30° onto a 12 μm thick Al foil. This drives fast electrons through the foil, generating a broadband Bremsstrahlung x-ray pulse from 10–100 keV, and upon exit at the rear surface, creates the conditions for ion acceleration via TNSA. The TNSA spectrum is a broadband Maxwellian pulse with tuneable cutoff energy [24,57]. The characteristics of the TNSA source produced by TARANIS are reported in [36]. Ionizing radiation is masked by a 500 μm wide slit incident normal to front surface of samples. The interaction is probed by a chirped pulse (200 ps–1.4 ns, 1053 nm), imaged with a 0.75 m imaging spectrometer for streak resolution (δ) of 0.33 ± 0.05 ps to 1.69 ± 0.25 ps (gray shaded region, Fig. 2). The decay constant τ_c is defined as the time taken for the opacity to recover to $1/e$ of its initial value. This was measured from traces using a weighted least squares fitting to the data and was carried out for different background subtractions. The total uncertainty on τ_c includes time of flight and background subtraction uncertainties. The spatial resolution is chosen in the range 2–20 μm depending on sample density and estimated proton energy.

Appendix B: Aerogels and anomalous diffusion—Silica aerogels consist of a porous network composed of individual silica nanoparticles that can be described as a mass fractal over lengths l_F, where $a < l_F < \xi_{ac}$. Unlike Euclidean (vector) space where dimension is always an integer, for fractals the dimension can be noninteger. Two important dimensions underpin the fractal phenomenology on these spatial scales. First, the Hausdorff, or fractal, dimension (D) describes how the geometrical distribution of the static structure scales with length. For aerogels $D = 1.8$ to 2.4 depending on the catalysis conditions. Second, the spectral, or fracton, dimension ($\bar{\bar{d}}$) describes the dynamic behavior of the mass fractal. Theoretically [12] $\bar{\bar{d}} = 4/3$ and has been found to be ~ 1.3 in experiments [43]. From these the exponent for anomalous diffusion is obtained from $d_w = 2D/\bar{\bar{d}}$ [40,41]. Therefore, in aerogels the inequality $2/d_w < 1$ always holds, implying significantly slower, or anomalous, diffusion is to be expected across the fractal network for spatial scales $< \xi_{ac}$.

Appendix C: Self-trapped exciton (STE) states in SiO_2—Trapping in STE states in bulk SiO_2 has been studied for irradiation with optical [47], x rays [58], and with protons [25], verifying the ultrafast decay pathway ($\tau_c < 0.45$ ps) is available to all species provided energy density is sufficiently low. Experiments using a focusing beam of optical radiation have placed a threshold $n_e^{\text{Exiton}} \sim 10^{20}$ cm^{-3} on the excited electron density for this pathway to dominate [50]. That work demonstrated as the fluence approaches the damage threshold in SiO_2 the vibrational amplitude on the lattice due to low viscosity modes is significantly greater than the lattice deformation required for STE trapping. Furthermore, these anharmonic lattice vibrations damp the phonon modes essential for electronic energy loss. Thus, ultrafast trapping in STE states is not possible for high density excitations. For lower excitation densities, where trapping is feasible, Martin *et al.* [48] established a strict criterion for STE formation: The electron must be within a distance R of the trapping site, where the Coulomb energy becomes greater than the thermal energy of the lattice. Therefore an electron with energy ~ 1 eV $\gg \frac{3}{2} k_B T$ requires $R < 0.5$ nm for trapping to be considered possible while for ~ 0.04 eV this increases to ~ 10 nm ($T = 300$ K).

Appendix D: Mean free path in SiO_2—In SiO_2 (~ 300 K) electrons excited into the conduction band by incident radiation initially lose energy rapidly via an impact ionisation cascade (e-e interaction) [59]. As the average electron energy (E_{av}) reduces to 10–20 eV, or subexcitation energies in SiO_2, scattering via quantized LO phonon emission [44] and continuous losses due to the reorientation of dipole molecules in the SiO_2 lattice or Deybe losses [45,46] start to dominate the stopping function. The resulting inelastic mean free path for electrons (λ_{IMFP}) is then given by Matheissen's rule ,

$$\frac{1}{\lambda_{IMFP}} = \frac{1}{\lambda_{II}} + \frac{1}{\lambda_{LO}} + \frac{1}{\lambda_{POL}} \tag{D1}$$

where, λ_{II}, λ_{LO}, and λ_{POL} are the mean free paths relating to impact ionization [59], LO phonon emission [44], and polaronic stopping [45,46], respectively. Fischetti [60] also showed how scattering from acoustic phonons is integral to this interaction. The well established result for λ_{IMFP} in bulk SiO_2 (density $\rho = 2.66$ g cm^{-3}) is given by the solid gray line in Fig. 4. Overall, this cascade enables the electron energy to approach the thermal energy of the lattice on ~ 0.1 ps timescales, with modeling [58] showing that this holds true for initial E_{av} extending to > 10 keV. This rapid equilibration [48] then permits the formation of STE states resulting in an ultrafast carrier lifetime of $\tau_{min} \sim 0.15$ ps [47].

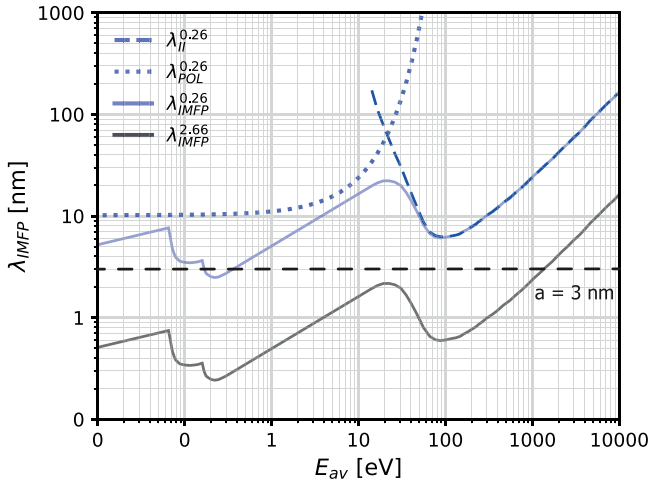

FIG. 4. Mean free paths for homogeneous density variation of SiO_2. The solid gray and blue lines show the mean free path $\lambda_{\mathrm{IMFP}}^{\rho_{\mathrm{av}}}$ for electrons interacting in bulk density SiO_2 with $\rho_{\mathrm{av}} = 2.66\ \mathrm{g\,cm^{-3}}$ and $\rho_{\mathrm{av}} = 0.26\ \mathrm{g\,cm^{-3}}$, respectively, assuming cross section σ independent of n for all interactions. Here, it is assumed that $\lambda_{\mathrm{IMFP}} \propto \rho_{\mathrm{av}}^{-1}$. Each $\lambda_{\mathrm{IMFP}}^{\rho_{\mathrm{av}}}$ is composed of the three main inelastic scattering mechanisms outlined in Eq. (D1). While impact ionization (λ_{II}, shown for $\rho_{\mathrm{av}} = 0.26\ \mathrm{g\,cm^{-3}}$) is dominant for $E_{\mathrm{av}} > 40$ eV, LO phonon scattering (λ_{LO}) and polaronic trapping [45] ($\lambda_{\mathrm{POL}} \propto e^{E_{\mathrm{av}}\gamma}$, with $\gamma = 0.085\ \mathrm{eV^{-1}}$ [46], shown for $\rho_{\mathrm{av}} = 0.26\ \mathrm{g\,cm^{-3}}$) become increasingly relevant for lower electron energies. The horizontal dashed line shows the mean nanoparticle diameter in the aerogel samples.

Appendix E: Hydrodynamic model—The thermal spike model describes a four-step process where incident ions transfer energy to target electrons, which is then shared among electrons, transferred to the lattice, and finally dissipated among atoms, resulting in an energy spike along the ion trajectory. The relaxation of the electron-hole plasma created around a proton track was modeled using a version of the semiconductor hydrodynamic model outlined in Klaumünzer [18]. For bulk SiO_2 we assume that within 10 fs the electron-hole plasma energy is distributed in a 5 nm wide Gaussian around the proton track, with the carriers having reached local thermal equilibrium. The equations of the hydrodynamic model were then solved from this initial condition using FEniCS [61]. Bulk simulations were performed on a 100 nm cube of density $2.66\ \mathrm{g\,cm^{-3}}$. For simulations on this timescale, trapping mechanisms have not been considered. For the aerogel simulations, a structure was created using the hierarchical cluster model described by Morales-Flórez *et al.* [62,63]. The resulting 100 nm cube of aerogel had density $0.26\ \mathrm{g\,cm^{-3}}$ and was meshed using a 3D finite element mesh generator, Gmsh [64]. Both aerogel and bulk simulations used the physical properties of bulk silica, i.e., band gap, thermal conductivity (see [27]).